Broadband wide-angle antireflection enhancement in AZO/Si shell/core subwavelength grating structures with hydrophobic surface for Si-based solar cells

Jung Woo Leem,[1] Young Min Song,[2] and Jae Su Yu[1,*]

[1]*Department of Electronics and Radio Engineering, Kyung Hee University, 1 Seocheon-dong, Giheung-gu, Yongin-si, Gyeonggi-do 446-701, Korea*

[2]*Department of Materials Science and Engineering, University of Illinois at Urbana-Champaign, Urbana, Illinois 61801, USA*

**jsyu@khu.ac.kr*

Abstract: Broadband wide-angle antireflection characteristics of aluminum-doped zinc oxide (AZO)/silicon (Si) shell/core subwavelength grating (SWG) structures with a hydrophobic surface, together with theoretical prediction using a rigorous coupled-wave analysis simulation, were investigated for Si-based solar cells. The AZO films with different thicknesses were deposited on Si SWGs by rf magnetron sputtering method, which forms a shell/core structure. The AZO/Si shell/core SWGs reduced significantly the surface reflection compared to the AZO films/Si substrate. The coverage of AZO films on Si SWGs improved the antireflective property over a wider incident angle. The AZO/Si shell/core SWG structure with a 200 nm-thick AZO layer deposited at an rf power of 200 W exhibited a water contact angle of 123°. This structure also exhibited a low average reflectance of ~2% over a wide wavelength range of 300-2100 nm with a solar weighted reflectance of 2.8%, maintaining a reflectance of < 9.2% at wavelengths of 300-2100 nm up to the incident angle of θ_i = 70°. The effective electrical properties of AZO films in AZO/Si shell/core SWGs were also analyzed.

OCIS codes: (050.6624) Subwavelength structures; (220.4241) Nanostructure fabrication; (310.1210) Antireflection coatings.

References and links

1. D. M. Braun, "Design of single layer antireflection coatings for InP/$In_{0.53}Ga_{0.47}As$/InP photodetectors for the 1200-1600 nm wavelength range," Appl. Opt. **27**(10), 2006–2011 (1988).
2. M. F. Schubert, F. W. Mont, S. Chhajed, D. J. Poxson, J. K. Kim, and E. F. Schubert, "Design of multilayer antireflection coatings made from co-sputtered and low-refractive-index materials by genetic algorithm," Opt. Express **16**(8), 5290–5298 (2008).
3. J. Zhao and M. A. Green, "Optimized antireflection coatings for high-efficiency silicon solar cells," IEEE Trans. Electron. Dev. **38**(8), 1925–1934 (1991).
4. N. Kadakia, S. Naczas, H. Bakhru, and M. Huang, "Fabrication of surface texture by ion implantation for antireflection of silicon crystals," Appl. Phys. Lett. **97**(19), 191912 (2010).
5. S. R. Kennedy and M. J. Brett, "Porous broadband antireflection coating by glancing angle deposition," Appl. Opt. **42**(22), 4573–4579 (2003).
6. J. Q. Xi, M. F. Schubert, J. K. Kim, E. F. Schubert, M. Chen, S. Y. Lin, W. Liu, and J. A. Smart, "Optical thin-film materials with low refractive index for broadband elimination of Fresnel reflection," Nat. Photonics **1**(3), 176–179 (2007).
7. S. Chhajed, M. F. Schubert, J. K. Kim, and E. F. Schubert, "Nanostructured multilayer graded-index antireflection coating for Si solar cells with broadband and omnidirectional characteristics," Appl. Phys. Lett. **93**(25), 251108 (2008).
8. G. K. Kiema, M. J. Colgan, and M. J. Brett, "Dye sensitized solar cells incorporating obliquely deposited titanium oxide layers," Sol. Energy Mater. Sol. Cells **85**(3), 321–331 (2005).

#149005 - $15.00 USD Received 9 Jun 2011; revised 25 Jul 2011; accepted 8 Aug 2011; published 23 Aug 2011

9. K. Robbie, D. J. Broer, and M. J. Brett, "Chiral nematic order in liquid crystals imposed by an engineered inorganic nanostructure," Nature **399**(6738), 764–766 (1999).
10. Y. J. Lee, D. S. Ruby, D. W. Peters, B. B. McKenzie, and J. W. P. Hsu, "ZnO nanostructures as efficient antireflection layers in solar cells," Nano Lett. **8**(5), 1501–1505 (2008).
11. Y. B. Tang, Z. H. Chen, H. S. Song, C. S. Lee, H. T. Cong, H. M. Cheng, W. J. Zhang, I. Bello, and S. T. Lee, "Vertically aligned p-type single-crystalline GaN nanorod arrays on n-type Si for heterojunction photovoltaic cells," Nano Lett. **8**(12), 4191–4195 (2008).
12. K. Peng, Y. Xu, Y. Wu, Y. Yan, S. T. Lee, and J. Zhu, "Aligned single-crystalline Si nanowire arrays for photovoltaic applications," Small **1**(11), 1062–1067 (2005).
13. P. Yu, C. H. Chang, C. H. Chiu, C. S. Yang, J. C. Yu, H. C. Kuo, S. H. Hsu, and Y. C. Chang, "Efficiency enhancement of GaAs photovoltaics employing antireflective indium tin oxide nanocolumns," Adv. Mater. **21**(16), 1618–1621 (2009).
14. O. K. Varghese, M. Paulose, and C. A. Grimes, "Long vertically aligned titania nanotubes on transparent conducting oxide for highly efficient solar cells," Nat. Nanotechnol. **4**(9), 592–597 (2009).
15. C. Lee, S. Y. Bae, S. Mobasser, and H. Manohara, "A novel silicon nanotips antireflection surface for the micro Sun sensor," Nano Lett. **5**(12), 2438–2442 (2005).
16. Y. M. Song, S. J. Jang, J. S. Yu, and Y. T. Lee, "Bioinspired parabola subwavelength structures for improved broadband antireflection," Small **6**(9), 984–987 (2010).
17. J. W. Leem, Y. M. Song, Y. T. Lee, and J. S. Yu, "Effect of etching parameters on antireflection properties of Si subwavelength grating structures for solar cell applications," Appl. Phys. B **100**(4), 891–896 (2010).
18. S. A. Boden and D. M. Bagnall, "Tunable reflection minima of nanostructured antireflective surfaces," Appl. Phys. Lett. **93**(13), 133108 (2008).
19. M. Y. Chiu, C. H. Chang, M. A. Tsai, F. Y. Chang, and P. Yu, "Improved optical transmission and current matching of a triple-junction solar cell utilizing sub-wavelength structures," Opt. Express **18**(S3), A308–A313 (2010).
20. M. C. Y. Huang, Y. Zhou, and C. J. Chang-Hasnain, "A surface-emitting laser incorporating a high-index-contrast subwavelength grating," Nat. Photonics **1**(2), 119–122 (2007).
21. Z. Yu, H. Gao, W. Wu, H. Ge, and S. Y. Chou, "Fabrication of large area subwavelength antireflection structures on Si using trilayer resist nanoimprint lithography and liftoff," J. Vac. Sci. Technol. B **21**(6), 2874–2877 (2003).
22. H. Kikuta, H. Toyota, and W. Yu, "Optical elements with subwavelength structured surfaces," Opt. Rev. **10**(2), 63–73 (2003).
23. J. W. Leem, Y. M. Song, Y. T. Lee, and J. S. Yu, "Antireflective properties of AZO subwavelength gratings patterned by holographic lithography," Appl. Phys. B **99**(4), 695–700 (2010).
24. T. Minami, "Transparent conducting oxide semiconductors for transparent electrodes," Semicond. Sci. Technol. **20**(4), S35–S44 (2005).
25. S. R. Kurtz and R. G. Gordon, "Transparent conducting electrodes on silicon," Sol. Energy Mater. **15**(4), 229–236 (1987).
26. J. W. Leem and J. S. Yu, "Glancing angle deposited ITO films for efficiency enhancement of a-Si:H/μc-Si:H tandem thin film solar cells," Opt. Express **19**(S3), A258–A268 (2011).
27. D. Kim, I. Yun, and H. Kim, "Fabrication of rough Al doped ZnO films deposited by low pressure chemical vapor deposition for high efficiency thin film solar cells," Curr. Appl. Phys. **10**(3 S1), S459–S462 (2010).
28. O. Lupan, S. Shishiyanu, V. Ursaki, H. Khallaf, L. Chow, T. Shishiyanu, V. Sontea, E. Monaico, and S. Railean, "Synthesis of nanostructured Al-doped zinc oxide films on Si for solar cells applications," Sol. Energy Mater. Sol. Cells **93**(8), 1417–1422 (2009).
29. T. Mizuta, T. Ishibashi, T. Minemoto, H. Takakura, and Y. Hamakawa, "Chemical deposition of zinc oxide thin films on silicon substrate," Thin Solid Films **515**(4), 2458–2463 (2006).
30. F. Chaabouni, M. Abaab, and B. Rezig, "Characterization of n-ZnO/p-Si films grown by magnetron sputtering," Superlattices Microstruct. **39**(1–4), 171–178 (2006).
31. O. Kluth, B. Rech, L. Houben, S. Wieder, G. Schöpe, C. Beneking, H. Wagner, A. Löffl, and H. W. Schock, "Texture etched ZnO:Al coated glass substrates for silicon based thin film solar cells," Thin Solid Films **351**(1–2), 247–253 (1999).
32. Y. Tak and K. Yong, "Controlled growth of well-aligned ZnO nanorod array using a novel solution method," J. Phys. Chem. B **109**(41), 19263–19269 (2005).
33. J. Y. Chen and K. W. Sun, "Growth of vertically aligned ZnO nanorod arrays as antireflection layer on silicon solar cells," Sol. Energy Mater. Sol. Cells **94**(5), 930–934 (2010).
34. J. Xiao, Y. Wu, X. Bai, W. Zhang, and L. Yu, "Controlled growth of ZnO pyramid arrays with nanorods and their field emission properties," J. Phys. D Appl. Phys. **41**(13), 135409 (2008).
35. S. A. Boden and D. M. Bagnall, "Optimization of moth-eye antireflection schemes for silicon solar cells," Prog. Photovolt. Res. Appl. **18**(3), 195–203 (2010).
36. S. K. Srivastava, D. Kumar, P. K. Singh, M. Kar, V. Kumar, and M. Husain, "Excellent antireflection properties of vertical silicon nanowire arrays," Sol. Energy Mater. Sol. Cells **94**(9), 1506–1511 (2010).
37. M. G. Moharam, "Coupled-wave analysis of two-dimensional gratings," Proc. SPIE **883**, 8–11 (1988).
38. A. J. Jääskeläinen, K. E. Peiponen, J. Räty, U. Tapper, O. Richard, E. I. Kauppinen, and K. Lumme, "Estimation of the refractive index of plastic pigments by Wiener bounds," Opt. Eng. **39**(11), 2959–2963 (2000).

#149005 - $15.00 USD Received 9 Jun 2011; revised 25 Jul 2011; accepted 8 Aug 2011; published 23 Aug 2011

39. D. G. Stavenga, S. Foletti, G. Palasantzas, and K. Arikawa, "Light on the moth-eye corneal nipple array of butterflies," Proc. Biol. Sci. **273**(1587), 661–667 (2006).
40. J. S. Hur, J. B. Song, J. Kim, D. Byun, C. S. Son, J. H. Yun, and K. H. Yoon, "Efficiencies of CIGS solar cells using transparent conducting Al-doped ZnO window layers as a function of thickness," J. Korean Phys. Soc. **53**(1), 437–441 (2008).
41. K. C. Sahoo, Y. Li, and E. Y. Chang, "Shape effect of silicon nitride subwavelength structure on reflectance for silicon solar cells," IEEE Trans. Electron. Dev. **57**(10), 2427–2433 (2010).
42. Y. Yang, X. Zeng, Y. Zeng, L. Liu, and Q. Chen, "Deposition of quasi-crystal Al-doped ZnO thin films for photovoltaic device applications," Appl. Surf. Sci. **257**(1), 232–238 (2010).
43. M. I. Mendelson, "Average grain size in polycrystalline ceramics," J. Am. Ceram. Soc. **52**(8), 443–446 (1969).
44. H. Wang, M. H. Xu, J. W. Xu, M. F. Ren, and L. Yang, "Low temperature synthesis of sol–gel derived Al-doped ZnO thin films with rapid thermal annealing process," J. Mater. Sci. Mater. Electron. **21**(6), 589–594 (2010).
45. H. Tong, Z. Deng, Z. Liu, C. Huang, J. Huang, H. Lan, C. Wang, and Y. Cao, "Effects of post-annealing on structural, optical and electrical properties of Al-doped ZnO thin films," Appl. Surf. Sci. **257**(11), 4906–4911 (2011).
46. J. Zhu, C. M. Hsu, Z. Yu, S. Fan, and Y. Cui, "Nanodome solar cells with efficient light management and self-cleaning," Nano Lett. **10**(6), 1979–1984 (2010).
47. J. Wang and L. L. Shaw, "Transparent nanocrystalline hydroxyapatite by pressure-assisted sintering," Scr. Mater. **63**(6), 593–596 (2010).
48. D. Buie, M. J. McCann, K. J. Weber, and C. J. Dey, "Full day simulations of anti-reflection coatings for flat plate silicon photovoltaics," Sol. Energy Mater. Sol. Cells **81**(1), 13–24 (2004).
49. B. Thaidigsmann, A. Wolf, and D. Biro, "Accurate determination of the IQE of screen printed silicon solar cells by accounting for the finite reflectance of metal contacts," Proc. 24th European PV Solar Energy Conference and Exhibition, Hamburg, Germany, 21–25 September (2009).

1. Introduction

Antireflection coatings (ARCs) have been widely used to improve the efficiency by reducing the Fresnel reflection loss at the surface in a variety of optoelectronic device applications such as optical sensors, photodetectors, and solar cells [1–3]. The performance of conventional ARCs including a single layer and multilayer thin-film stacks is typically limited to a small range of incidence angles and a narrow bandwidth [4]. The nanoporous structures with air gaps of dielectric materials (e.g., SiO_2, TiO_2, MgF_2) by an oblique angle deposition were demonstrated for a more broadband antireflection property [5–9]. Nowadays, various nanostructures, such as nanorods, nanowires, nanotubes, and nanotips, which produce a refractive index gradient between air and the material by a volume density gradient, were proposed to suppress the surface reflection [10–15]. However, most nanostructures approximated as disordered structures make it somewhat difficult to obtain the desired refractive index profile and often experience the serious light scattering. In contrast, periodic subwavelength gratings (SWGs), which have a period smaller than the incident light wavelength, give us effective control over the surface relief profile to enhance the amount of light coupled into the absorption layer in the wide ranges of wavelengths and incident angles for photovoltaic applications [16–19]. In general, electron-beam or nanoimprint lithography has been used for the periodic nanopatterning of SWGs, but it is complicated and expensive process [20,21]. As an alternative, holographic lithography using laser beam interference can be employed as a simple, fast, and cost-effective patterning technique over a large area [22,23].

Particularly, in silicon (Si)-based solar cells, the key issue is to reduce the surface reflection because of the high refractive index change at the air/Si interface and low absorption. In practical devices, transparent conductive oxides (TCOs) on the top of the semiconductor were usually used for transparent electrodes as well as ARCs due to the good optical and electrical properties [24–26]. Among TCOs, the aluminum-doped zinc oxide (AZO) with a wide bandgap has been widely studied for Si-based solar cells due to low cost, chemical/thermal stability, non-toxicity, and resistance to the hydrogen plasma [27,28]. Unfortunately, the ZnO film/Si structures show a high reflectivity with strong oscillations [29,30]. Recently, textured ZnO films, ZnO nanorods, and ZnO pyramidal arrays, which are the disordered structures, are attracting growing interest for ZnO ARCs [31–34]. However, the investigation of transparent conducting ZnO ARCs with a periodic nanostructure has been

#149005 - $15.00 USD Received 9 Jun 2011; revised 25 Jul 2011; accepted 8 Aug 2011; published 23 Aug 2011

rarely reported. Also, the coverage of ZnO with a low refractive index on high refractive index semiconductors would modify the refractive index profile, which changes the reflection characteristics. On the other hand, for the textured surface in ARCs of solar cells, it is necessary to be well passivated to minimize the surface recombination loss which becomes larger with increasing the surface area [35]. For periodic SWG structures, the surface recombinaiton effect would be relatively low compared to the disordered nanostructures such as nanowires and nanorods due to their smaller surface area [36]. Moreover, the self-cleaning super-hydrophobic surface is commonly required for solar cell applications. Thus, it is very meaningful to analyze the surface reflection and water wettability by applying SWG structures to AZO/Si substrate. In this work, we investigated the structural, optical, and electrical properties and water wetting behavior of the AZO/Si shell/core SWG structures, which were fabricated by laser interference lithography, inductively coupled plasma (ICP) etching, and subsequent rf magnetron sputtering, to achieve a broadband wide-angle antireflection and surface self-cleaning functionality for Si-based solar cell applications.

2. Experimental details

Figure 1 shows the schematic illustration of process steps for the fabrication of AZO/Si shell/core SWG structures. The corresponding top-view, oblique-view, and cross-sectional scanning electron microscope (SEM) images of the fabricated Si SWG and AZO/Si shell/core SWG structures are also shown. For the fabrication of the Si SWG structure, the details can be found in our previous work [17]. To fabricate the Si SWG structures, the photoresist (PR) was spin-coated on semi-insulating Si substrates with a size of 2×2 cm^2. The thickness of the coated PR was roughly 180 nm. The prebaking on a hot plate was carried out at 90 °C for 90 s. For subwavelength scale etch mask with two-dimensional periodic hexagonal patterns, the PR was exposed twice with 60° sample rotation between exposures by the interference of two laser beams using a 363.8 nm Ar ion laser. After the development, the SWG structures were fabricated on a Si surface through the pattern transfer using ICP (Plasmalab System 100, Oxford) etching in $SiCl_4$ plasma. The tapered conical Si SWG structure can be fabricated by the $SiCl_4$-based ICP etching process, depending on the etching conditions [17]. The overall etching of PR patterned samples provides extremely fast etching at the rim and slower etching at the center, thus resulting in a tapered profile structure. The ICP process at a low rf power of 25 W was performed to obtain the Si SWG structure with a smooth tapered profile until complete removal of PR patterns on the Si substrate. The flow rate of $SiCl_4$ gas and the process pressure were 5 sccm and 10 mTorr, respectively. The top-view SEM image of fabricated Si SWG confirms the closely packed hexagonal patterns.

To optimize the AZO as a TCO on the Si SWGs, the AZO films were deposited by a rf magnetron sputtering system at different process conditions under 1×10^{-6} Torr base pressure. The sputtering process was performed at room temperature. The ZnO:Al (5N, 2 wt.% Al_2O_3) target was used. The target to substrate distance was 20 cm and the process pressure was 5 mTorr in an Ar environment. The rf power was changed from 100 to 200 W. For a good uniformity, the samples were rotated with 20 rpm during the sputtering. The AZO thin films were prepared at thicknesses of 100, 200, 300, and 500 nm. For the fabricated samples after the deposition process, there was no additional heat treatment. The etched profile and surface morphology of the fabricated AZO/Si shell/core SWG structures were observed by using a SEM (LEO SUPRA 55, Carl Zeiss). The optical reflectance was measured by using a UV-VIS-NIR spectrophotometer (Cary 5000, Varian). The samples were mounted to their backside with an angle of ~8° (near-normal incidence) with respect to the linearly polarized incident light. For angle-dependent reflectance measurement, a Cary variable angle specular reflectance accessory in a specular mode was used. The crystallinity and orientation of samples were analyzed by X-ray diffraction (XRD, M18XHF-SRA, Mac Science) measurements using the monochromated Cu Kα line source ($\lambda = 0.154178$ nm). The effective electrical properties (i.e., resistivity, carrier concentration, and Hall mobility) of the AZO thin

#149005 - $15.00 USD Received 9 Jun 2011; revised 25 Jul 2011; accepted 8 Aug 2011; published 23 Aug 2011

films deposited on Si SWG structures were determined by using a Hall effect measurement system (HL5500PC, Accent). The contact angles of water droplets on the surfaces were taken by using a contact angle measurement system (Phoenix-300, SEO Co., Ltd.).

For theoretical analysis, the reflectance calculations were carried out using a rigorous coupled-wave analysis (RCWA) simulation [37]. We assume that the linearly polarized incident light enters from air into the structure at normal incidence ($\theta_i = 0°$). The fifth order of diffraction, which is a sufficient number to stabilize the results numerically, is also used to calculate the diffraction efficiency in simulations.

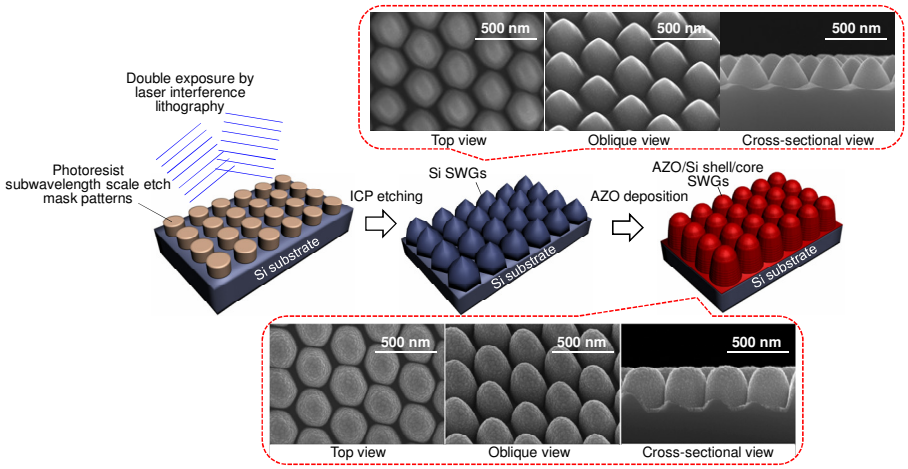

Fig. 1. Schematic illustrations and SEM images corresponding to process steps for the fabrication of AZO/Si shell/core SWG structures. The oblique-view SEM images are taken at a 30° tilt angle.

3. Results and discussion

Figure 2 shows the (a) schematic illustrations and calculated effective refractive index profiles, (b) calculated reflectance spectra, and (c) contour plots of the calculated incident angle dependent reflectance in the wavelength range of 300-2100 nm for (i) AZO films/Si substrate and (ii) AZO/Si shell/core SWGs with a 100 nm-thick AZO, respectively. The insets of Fig. 2(b) show a three-dimensional model of the AZO/Si shell/core SWGs with a 6-fold hexagonal symmetry structure, which is estimated from the SEM image, and the effective refractive index distribution of the AZO/Si shell/core SWG structure used in this simulation. The period and height of AZO/Si shell/core SWGs are 300 and 380 nm, respectively. The effective refractive index can be calculated using a volume weighted average of the refractive indices of the different constituents [38]. For AZO films/Si substrate, the effective refractive index changes abruptly from ~3.8 (n_{Si}) to 1 (n_{air}) via ~1.89 (n_{AZO}) across the AZO film interfaces. In contrast, the tapered SWGs can create a gradient effective refractive index between the material and air as observed from the moth eye effect [39]. As calculated in Fig. 2(a), the effective refractive index of parabola-like AZO/Si shell/core SWG structure is almost linearly changed from air to the Si substrate via the AZO/Si shell/core SWG, thus relaxing the abrupt refractive index change in the AZO film/Si substrate. The reflectance of AZO/Si shell/core SWG structure is significantly reduced compared to the AZO film/Si substrate due to the linearly graded refractive index profile, resulting in the reflectance values below than 15.3% over a wide wavelength region of 300-2100 nm. As shown in Fig. 2(c), for AZO/Si shell/core SWG structure, the reflectance is much less dependent on the incident angle over a wide wavelength of 300-2100 nm than that of the AZO film/Si substrate. The reflectance remains almost the same, i.e., < 5%, at wavelengths of 300-2100 nm except for around 470 nm up to $\theta_i = 50°$ and still low despite the high incident angle of $\theta_i = 70°$. Thus, the AZO/Si

#149005 - $15.00 USD Received 9 Jun 2011; revised 25 Jul 2011; accepted 8 Aug 2011; published 23 Aug 2011

shell/core SWG structure is expected to serve as a TCO with efficient broadband wide-angle antireflection property on the Si absorption layer.

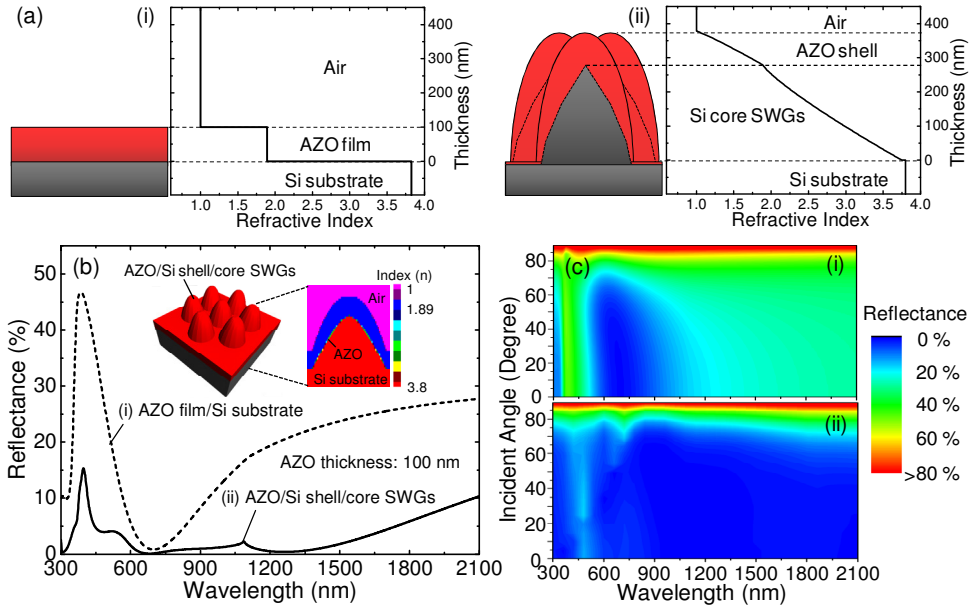

Fig. 2. (a) Schematic illustrations and calculated effective refractive index profiles, (b) calculated reflectance spectra, and (c) contour plots of the calculated incident angle dependent for (i) AZO films/Si substrate and (ii) AZO/Si shell/core SWGs with a 100 nm-thick AZO, respectively. The insets of (b) show a three-dimensional model of the AZO/Si shell/core SWGs with a 6-fold hexagonal symmetry structure and the effective refractive index distribution of the AZO/Si shell/core SWG structure used in this simulation.

Figure 3 shows the (a) SEM images and (b) measured reflectance spectra of the AZO/Si shell/core SWG structures with AZO thicknesses of (i) 100 nm, (ii) 200 nm, (iii) 300 nm, and (iv) 500 nm. The insets of Fig. 3(a) show the cross-sectional SEM images of the corresponding structures. The rf power is 100 W and the period of SWGs is 300 nm. The surface of Si SWGs was completely filled with the AZO by the sputtering. As the thickness of AZO was increased to 200 nm, the shape of the AZO/Si shell/core SWG structure became more parabola-like with a higher height, and then turned into films consisting of columnar structures with a further increase. The average height of AZO/Si shell/core SWGs was also increased from 375 nm at 100 nm-thick AZO to 768 nm at 500 nm-thick AZO. For comparison, the measured reflectance spectra of the AZO films/Si substrate with AZO thicknesses of 100, 200, 300, and 500 nm are shown in the inset of Fig. 3(b). For AZO of 100 nm, the measured reflectance spectra for both structures are reasonably consistent with the calculated results as shown in Fig. 2(b). In the AZO film (100 nm)/Si substrate, the reflectance was significantly higher except for the wavelength region of near 700-800 nm, thus leading to an average reflectance of ~19% at wavelengths of 300-2100 nm. As the thickness of AZO film on Si substrate was increased, the interference oscillations of the reflectance spectra became larger. The average reflectance was decreased to 11.4% at 300-2100 nm for AZO film (500 nm)/Si substrate because the absorption rate of the thicker film is higher than the reflection rate [40]. From this, the AZO film with a desirable thickness as a transparent electrode layer should be chosen for solar cell applications by considering the optical and electrical properties. For AZO/Si shell/core SWG structures, the reflectance was reduced considerably compared to the AZO films/Si substrate due to the gradient in the effective refractive index as mentioned above. In the case of the AZO (100 nm)/Si shell/core

#149005 - $15.00 USD Received 9 Jun 2011; revised 25 Jul 2011; accepted 8 Aug 2011; published 23 Aug 2011

SWG structure, the reflectance was further reduced at 600-1100 nm, which was similar to the calculated results in Fig. 2(b). The interference oscillations were also increased gradually for thicker AZO because the AZO deposited on Si SWGs became film-like structures as shown in Fig. 3(a). The average reflectance was slightly increased from ~4% at wavelengths of 300-2100 nm for the AZO/Si shell/core SWG with AZO of 100 nm to ~5.1% for that with AZO of 500 nm in spite of the increased AZO thickness. For AZO film (200 nm)/Si substrate, the average reflectance was 14.1% at wavelengths of 300-2100 nm. Whereas, the parabola-shaped AZO (200 nm)/Si shell/core SWG structure with a high average height of 476 nm exhibited the lowest average reflectance of 3% at 300-2100 nm. This can be explained by the fact that the parabola-like AZO/Si shell/core SWG structure with a higher height, which has a linearly graded refractive index profile, results in a relatively lower surface reflectance [18,39,41].

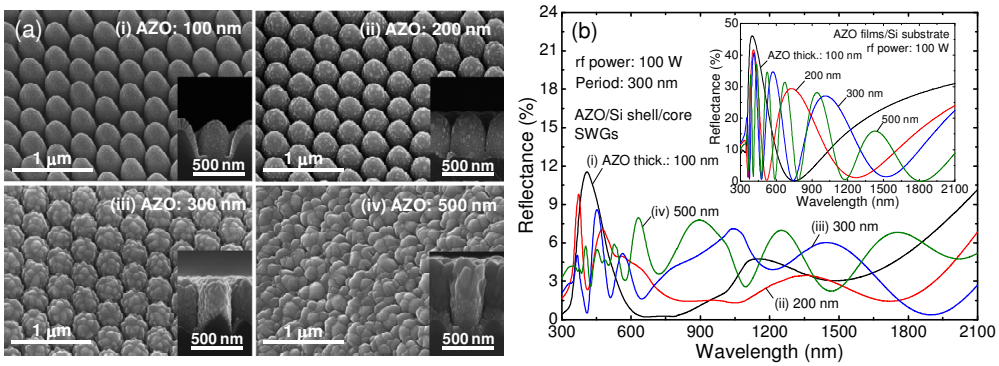

Fig. 3. (a) SEM images and (b) measured reflectance spectra of the AZO/Si shell/core SWG structures with AZO thicknesses of (i) 100 nm, (ii) 200 nm, (iii) 300 nm, and (iv) 500 nm. The insets of (a) and (b) show the cross-sectional SEM images of the corresponding structures and measured reflectance spectra of the AZO films/Si substrate with AZO thicknesses of 100, 200, 300, and 500 nm, respectively. The period of SWGs is 300 nm.

Figure 4(a) shows the measured reflectance spectra of AZO (200 nm)/Si shell/core SWGs for different periods in the wavelength region of 300-2100 nm. The insets show the SEM images of the corresponding structures. The AZO films were deposited at the rf power of 100 W. The period of AZO/Si shell/core SWGs can be changed by tuning the rotation stage angle in the laser interference lithography process. The reflectance spectra depend on the period of AZO/Si shell/core SWG structures. The reduced packing density of SWGs increased the reflectance for the larger period as shown in of Fig. 4(a). With the increasing the period of SWGs, the low-reflectance band shifted roughly towards the longer-wavelength region at wavelengths of around 450, 900, and 1800 nm and its minimum values were gradually increased. The influence of the period in AZO (200 nm)/Si shell/core SWGs with a 6-fold hexagonal array on the calculated reflectance as a function of the wavelength is shown in Fig. 4(b). As the period of the AZO/Si shell/core SWGs increases, the low reflectance band (< 2%) broadens and shifts toward higher wavelengths and it is also split into several regions [16]. This shows a similar tendency as the experimental data though there is a discrepancy between the measured and calculated results at some wavelengths due to the difficulty in matching exactly the geometric simulation model to the fabricated structure. In simulations, for periods of 450-500 nm, the AZO/Si shell/core SWGs maintain the low reflectance below 2% over a wide wavelength region of 400-2100 nm. This indicates that the low reflectance region can be controlled by adjusting the period of AZO/Si shell/core SWGs.

#149005 - $15.00 USD Received 9 Jun 2011; revised 25 Jul 2011; accepted 8 Aug 2011; published 23 Aug 2011

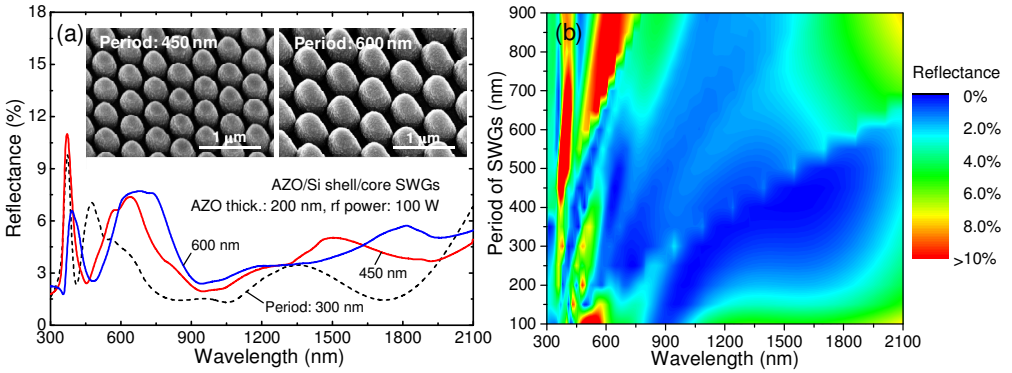

Fig. 4. (a) Measured reflectance spectra of AZO (200 nm)/Si shell/core SWGs for different periods and (b) influence of the period of AZO (200 nm)/Si shell/core SWGs with a 6-fold hexagonal array on the calculated reflectance as a function of the wavelength. The insets of (a) show the SEM images of the corresponding structures.

Figure 5(a) shows the SEM images of the AZO (200 nm)/Si shell/core deposited at rf powers of (i) 100 W, (ii) 150 W, and (iii) 200 W for the period of 300 nm. The 2θ scan XRD patterns of the corresponding structures for different rf powers are shown in the (iv) of Fig. 5(a). The deposition rate of AZO films was increased with increasing the rf power due to the more argon ions to bombard on the target and they were 6.3, 9.7, and 12.3 nm/min at 100, 150, and 200 W, respectively. For 200 nm-thick AZO, the outer shells of AZO on the tapered conical Si core SWGs have a parabola-like shape. From the SEM images, it can be observed that the number of grain boundaries visible on the surface of the AZO was reduced as the rf power was increased. As shown in (iv) of Fig. 5(a), the diffraction peaks from (002), (101), and (102) plane orientations were observed. As the rf power was increased, the (002) XRD peak intensity, i.e., the c-axis of the hexagonal wurtzite structure, became larger and the (102) intensity peak got lower at higher rf power, whereas the (101) XRD peak remained almost the same. The measured XRD patterns confirm that the grain size of AZO shells is increased and its crystallinity is improved with rf power [42]. The grain size (D) can be estimated using Scherrer formula [43], $D = 0.9\lambda/(\beta\cos\theta)$, where λ is the wavelength of the X-ray, β is the FWHM of the (002) XRD peak, and θ is the diffractive angle. The grain size was increased from 19.2 nm at rf power of 100 W to 30.8 nm at 200 W.

Figure 5(b) shows the effective resistivity (ρ), carrier concentration (n), and Hall mobility (μ) of the AZO film with a 200 nm-thick in AZO/Si shell/core SWGs as a function of rf power. In this measurement, indium contacts were deposited onto the surface of square-shaped samples with a size of 1 × 1 cm^2 in the Van der Pauw geometry. Then, the samples were heated on a hot plate at the temperature of 180 °C for 3 min. For AZO/Si shell/core SWG structures, the resistivity of AZO films was decreased from 3.77×10^{-2} Ω-cm at 100 W to 2.4×10^{-2} Ω-cm at 200 W with increasing the rf power. The improvement of electrical property may be attributed to the enhancement in grain size and crystallinity at the rf power of 200 W. It is noted that the grain boundary scattering is decreased as the grain size is increased, which also improves the transmission properties [44]. The Hall mobility was increased from 9.3 $cm^2V^{-1}s^{-1}$ at the rf power of 100 W to 12.1 $cm^2V^{-1}s^{-1}$ at 200 W. The carrier concentration was also increased from 1.78×10^{19} to 2.14×10^{19} cm^{-3} as the rf power was increased from 100 to 200 W. Thus, the decrease in resistivity is due mainly to the increased Hall mobility because the resistivity is proportional to the reciprocal of the product the Hall mobility and carrier concentration. Although the resistivity of AZO films on the SWG structures is somewhat higher than that (i.e., ~10^{-3} Ω-cm) of standard TCOs used on solar cells, it can be improved by the post-annealing process, which leads to an enhanced electrical properties of the AZO films [44,45].

#149005 - $15.00 USD Received 9 Jun 2011; revised 25 Jul 2011; accepted 8 Aug 2011; published 23 Aug 2011

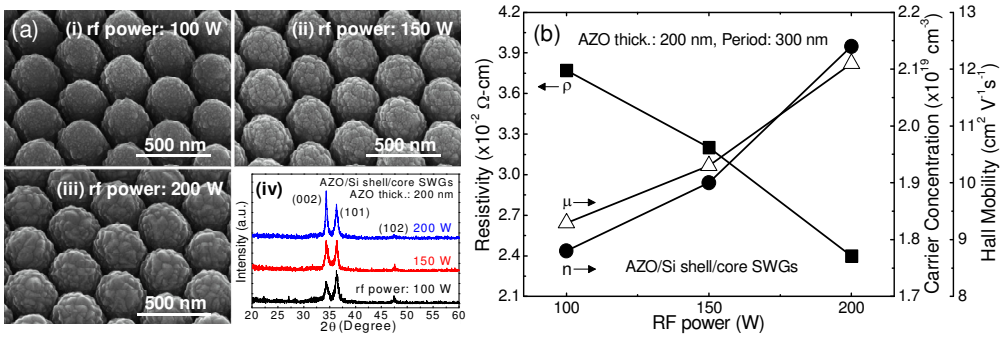

Fig. 5. (a) SEM images of the AZO (200 nm)/Si shell/core SWGs deposited at rf powers of (i) 100 W, (ii) 150 W, and (iii) 200 W. The (iv) of (a) shows the 2θ scan XRD patterns of corresponding structures for different rf powers. (b) Effective resistivity, carrier concentration, and Hall mobility of the AZO film with a 200 nm-thick in AZO/Si shell/core SWGs as a function of rf power.

Figure 6(a) shows the measured reflectance spectra of the AZO films/Si substrate and AZO/Si shell/core SWG structures with a 200 nm-thick AZO, respectively, deposited at rf powers of 100 and 200 W for the period of 300 nm. To determine the surface macroscopic properties on the wettability, the contact angles were measured. The insets show the photographs of water droplet shapes with contact angles on AZO film/Si substrate and AZO/Si shell/core SWGs with a 200 nm-thick AZO, respectively, deposited at an rf power of 200 W. For AZO film/Si substrate, the water droplet spread out, leading to a contact angle of 77° which is close to being the hydrophilic due to the flat surface; while for the AZO/Si shell/core SWG structure, the contact angle increased to 123° compared to the AZO film/Si substrate. This structure with a hydrophobic surface can self-clean the dust particles on the surface of solar cells in real environments [46]. The overall reflectance is slightly decreased when the rf power was increased from 100 to 200 W for both AZO film/Si substrate and AZO/Si shell/core SWG structure. The AZO/Si shell/core SWG deposited at the rf power of 200 W exhibited a low average reflectance of ~2%. This decrease of the reflectance may be attributed to the reduced optical scattering at grain boundaries caused by the increased grain size at higher rf power [44,47]. For solar cell applications, the solar weighted reflectance (SWR), i.e., the ratio of the useable photons reflected to the total useable photons, can be evaluated by normalizing the reflectance spectra with the internal quantum efficiency (IQE) spectra of a solar cell and the air mass 1.5 global (AM1.5g) spectrum [48]. The IQE spectrum of the experimentally reported Si-based solar cell was employed in the wavelength range of 300-1100 nm [49]. For 200 nm-thick AZO deposited at an rf power of 200 W, the SWR of AZO film/Si substrate was 18.2% but it considerably decreased to 2.8% for the AZO/Si shell/core SWG structure.

Figure 6(b) shows the measured angle-dependent reflection spectra of the AZO (200 nm)/Si shell/core SWGs deposited at an rf power of 200 W for the period of 300 nm. The insets show the photographs (left) of AZO film/Si substrate and AZO/Si shell/core SWGs, and the zoom-out SEM image (right) of AZO/Si shell/core SWGs. The surface of AZO/Si shell/core SWG structure appeared dark black because it absorbs light of a wide range of wavelengths and does not reflect the light compared to the AZO film/Si substrate, which indicates a very low surface reflectivity as confirmed in Fig. 6(a). It can be observed that the fabricated AZO/Si shell/core SWG structure was very uniform and closely-packed over a large area. To evaluate the omnidirectional antireflection characteristics of AZO/Si shell/core SWGs, the reflectance was measured for different incident angles (θ_i) from θ_i = 8° (near-normal incidence) to θ_i = 70°. As the incident angle of light was increased, the reflectance was not much increased up to θ_i = 50°. For large incident angle of θ_i = 70°, the reflectance remained as low values below 9.2% (average reflectance of < 7.8%) over a wide wavelength

#149005 - $15.00 USD Received 9 Jun 2011; revised 25 Jul 2011; accepted 8 Aug 2011; published 23 Aug 2011

range of 300-2100 nm. The measurement results showed similar trends to the simulated results in Fig. 2(c). For AZO/Si shell/core SWGs, a lower angle dependency of surface reflection can be achieved over a broad wavelength range compared to the AZO film/Si substrate.

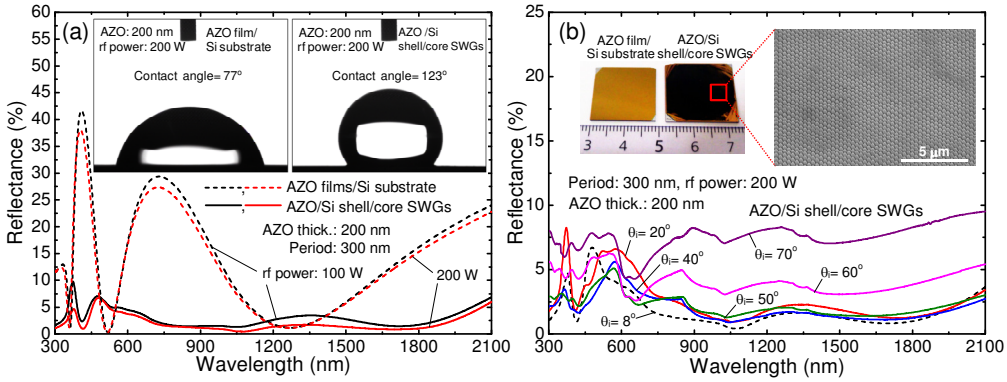

Fig. 6. (a) Measured reflectance spectra of the AZO films/Si substrate and AZO/Si shell/core SWG structures with a 200 nm AZO, respectively, deposited at rf powers of 100 W and 200 W and (b) measured angle-dependent reflection spectra of the AZO (200 nm)/Si shell/core SWGs deposited at an rf power of 200 W for the period of 300 nm. The insets of (a) show the photographs of water droplet shapes with contact angles on AZO film/Si substrate and AZO/Si shell/core SWGs with a 200 nm AZO, respectively, deposited at an rf power of 200 W. The insets of (b) show the photographs (left) of AZO film/Si substrate and AZO/Si shell/core SWGs, and the zoom-out SEM image (right) of AZO/Si shell/core SWGs.

4. Conclusion

The antireflective properties of AZO/Si shell/core SWG structures in comparison with AZO films/Si substrate over wide wavelength and incident angle regions were investigated experimentally and in theoretical studies using RCWA simulations. The structure profile of AZO on tapered conical Si SWGs turned into the parabola shapes in a closely packed array with increasing the thickness of deposited AZO film, and then films consisting of columnar structures. The reflectance was significantly decreased to an average reflectance of ~2% over a wide wavelength range of 300-2100 nm with a SWR of 2.8% for AZO/Si shell/core SWG structure with a high surface hydrophobicity (i.e., water contact angle of 123°) compared to AZO films/Si substrate. The electrical properties of the AZO in AZO (200 nm)/Si shell/core SWGs were enhanced with the increase of rf power during deposition due to the increased grain size. The omnidirectional antireflectance characteristics of AZO/Si shell/core SWGs were also improved compared to AZO film/Si substrate, exhibiting a less incident angle-dependent reflectance of < 9.2% at wavelengths of 300-2100 nm up to the incident angle of θ_i = 70°. These results can provide a better insight into the broadband wide-angle antireflection nanostructures with a self-cleaning hydrophobic surface for the fabrication of high-performance Si-based solar cells.

Acknowledgments

This research was supported by Basic Science Research Program through the National Research Foundation of Korea (NRF) funded by the Ministry of Education, Science and Technology (No. 2010-0016930).

#149005 - $15.00 USD Received 9 Jun 2011; revised 25 Jul 2011; accepted 8 Aug 2011; published 23 Aug 2011